

## Investigating the dielectric properties of PMMA/RGO nanocomposites using experimental techniques with artificial neural network ANN

### Model

**R. A. Mohamed<sup>1\*</sup>, M. Y. El-Bakry<sup>1</sup>, D. M. Habashy<sup>1</sup>, A. S. Mohamed<sup>1</sup>, A. M. Ismail<sup>1</sup>**

<sup>1</sup>Physics Department, Faculty of Education, Ain Shams University, Cairo, Egypt.

The current research introduces a combined investigation using both experimental methods and theoretical model to understand and predict the dielectric behavior of PMMA polymer nanocomposites. Poly (methyl methacrylate) (PMMA)/reduced graphene oxide (RGO) nanocomposite films with varying RGO nano-platelets (NPs) contents are made using the casting process. The dielectric constant  $\epsilon'$ , loss  $\epsilon''$ , ac-conductivity  $\sigma_{ac}$  of PMMA/RGO nanocomposites are investigated in the temperature range (300 K – 390 K) and frequency range (100 Hz – 1 MHz).  $\sigma_{ac}$  and the frequency exponent  $S$  are interpreted by the correlated barrier hopping CBH model. The frequency exponent  $S$  and charge carrier binding energy  $W_m$  in the nanocomposite films exhibit a decrease with increasing temperature and RGO content.  $\epsilon'$ ,  $\epsilon''$  and  $\sigma_{ac}$  of PMMA/RGO nanocomposites depend on both frequency  $f$  and temperature  $T$ . The study employed ANN as a soft-computing process to model the dielectric behavior of the investigated polymer nanocomposites. The measured experimental datasets served as inputs. The optimized ANN configuration was used to train the model for  $\epsilon'$ ,  $\epsilon''$  and  $\sigma_{ac}$ . ANN simulation results exhibited excellent fitting with the measured experimental data. Notably, the ANN not only accurately predicted experimental measurements (serving as a test step) but also successfully predicted values for unmeasured data points. To evaluate the model's performance, Mean Squared Error MSE was calculated. The consistently low MSE values (below 0.08) indicated a high degree of accuracy. Additionally, the correlation coefficient R provided further confirmation, with its value signifying a strong correlation between the ANN results and their targets. In conclusion, this research establishes the capability of ANN in modeling and predicting the dielectric characteristics of the studied polymer nanocomposites.

### Keywords

Polymer nanocomposites; dielectric properties; ac conductivity, and ANN model

\*: [Rashaali@edu.asu.edu.eg](mailto:Rashaali@edu.asu.edu.eg)

Receive Date: 6 February 2025; Revise Date: 3 March 2025; Accept Date: 25 March 2025; Publish: 14 April 2025

## **1. Introduction**

Dielectric nanocomposites with outstanding dielectric properties have gained significant attention due to their vast use, which includes dielectric condensers, hybrid electric cars, and optoelectronic devices [1, 2]. Polymeric composites can provide perfect dielectric materials with high dielectric constant  $\epsilon'$ , low dielectric loss  $\epsilon''$ , and high mechanical strength. These materials are flexible, mechanically stable, and easy to process and produce [3]. Polymethyl methacrylate (PMMA) is a linear, flexible, thermoplastic, transparent colorless, and nontoxic polymeric material with an ester group. However, its low dielectric constant and conductivity limit its usefulness in a variety of applications. PMMA is one of the best polymers for filler dispersion because of its amorphous form and chemical and abrasion resistance [4,5]. One of the most well-known strategies of polymer modification is the combination of two or more components having distinct characteristics [6]. Adding nanofillers to polymers is an appealing way for creating novel polymer nanocomposites with specific features without having to synthesize whole new materials. PMMA is widely employed in a variety of technical applications due to its unique combination of superior optical, mechanical, and electrical qualities, thermal stability, weather resistance, and ease of shape. PMMA is a top-performing organic optical material. It has been used to produce a range of optical devices, including optical lenses [7].

Reduced graphene oxide (RGO), a two-dimensional version of graphite, has received a lot of attention because of its large surface area, conductivity, and outstanding mechanical qualities. Reduced graphene oxide (RGO) nanoplatelets are formed of single sheets of reduced graphite oxide with some functional groups such as hydroxyl and carboxyl on the basal planes and edges [8]. Because of its high compatibility with polymers, RGO is an excellent material for the synthesis of functional nanocomposites [9]. Furthermore, RGO has a greater specific surface area, high chemical potential, superior chemical stability, and a diverse drape morphology [10]. Poly(methyl methacrylate) (PMMA) and reduced graphene oxide (RGO) are two versatile materials that, when combined, form a unique nanocomposite with improved properties and a wide range of applications, including supercapacitors, flexible electronics, pressure sensors, temperature sensors, microelectromechanical systems, and optoelectronic devices.

Soft computing techniques have become important in many applications for different fields. They achieve the integration among practical/theoretical areas. During an experiment, various difficulties face the researcher: the cost of the consumed materials, and the restrictions of some laboratories' equipment. So modeling is utilized to describe and forecast the property of systems and is used in various scientific disciplines. Modeling using learning algorithms has an excellent role in forecasting different properties [11-13]. Making predictions decrease the experimental samples for investigation saving time and money. ANN model is a machine-learning process that relies on the human learning technique that exhibits many advantages: fast training, easy to use, treating nonlinear

problems, and high learning rates. So, many researches were conducted in modeling of the different properties of materials based on ANN model [14–20].

Utilization of ANN for estimating electric, magnetic, and different physical and chemical characteristics of polymers is introduced by [21-26]. Although those research attempts are increasing rapidly, there is still a need for an extensive gain of the capabilities of ANN. The current research intends to apply the ANN model in a new promising area. The main goal is to experimentally investigate the dielectric-characteristics of PMMA/RGO nanocomposite. The measurements are performed at different temperatures  $T$  in the frequency  $f$  limits from 100 to 1MHz. Then, ANN is employed to model and predict the dielectric behavior of the understudy polymer. Finally, ANN equation is obtained to describe the behavior and experimentally predict unmeasured values.

Traditional models for predicting dielectric properties may struggle with the complex, nonlinear relationships present in nanocomposites. The use of an ANN could provide a significantly more accurate predictive model, especially when considering variables like RGO concentration, temperature, and frequency. Novelty can be found in the ANN architecture itself. An example is creating a new ANN architecture that is designed specifically for nanocomposite dielectric properties. By combining experimental data with ANN analysis, the study could reveal previously unknown correlations between the microstructure of the nanocomposite and its dielectric behavior. The ANN could help to identify critical parameters that have the most significant impact on dielectric properties, leading to optimized material design. The study is structured into five sections. The first section provides essential information and introduces the core research question. The following section introduces the details of the practical procedures. Next, section three establishes ANN fundamentals. Section four dives into the results, offering a comprehensive discussion and comparing the ANN's predictions with the experimentally obtained data. The last section introduces the concluding remarks.

## 2. Experimental

### 2.1. Materials and samples preparation

Poly (methyl methacrylate) (PMMA)  $[\text{CH}_2\text{C}(\text{CH}_3)(\text{CO}_2\text{CH}_3)]_n$  (average Mw ~350,000 g/mol by GPC) with density of  $1.18 \text{ g/cm}^3$  and reduced graphene oxide RGO nanoplatelets of mean particle size ( $< 200 \text{ nm}$ ) and density of  $0.3 \text{ g/cm}^3$  were supplied from Sigma Aldrich. Tetrahydrofuran (THF)  $\text{C}_4\text{H}_8\text{O}$  (Mw ~ 72.11 g/mol) was applied as a solvent with purity of 99.8% from (Fisher Scientific). Tetrahydrofuran (THF) is an organic, colorless, volatile polar solvent used in the production of various polymers. The PMMA chains are thought to be randomly arranged because the interactions between them were weakened by their interactions with THF and consequently maintain the amorphous structure of PMMA. Nanocomposite films were prepared by the solution casting method. Firstly, 10 g of PMMA were dissolved in THF at room temperature (RT), stirring for 6

## **R. A. Mohamed et al.**

hours until the polymer was full dissolved. Secondly, RGO NPs were also suspended in THF by sonication for 30 minutes, then the required contents (0.25, 0.5, 1.0, and 2.0 wt.%) of RGO NPs were added to the PMMA solution under stirring for 2 hours and sonicated for 30 mins to ensure the good NPs homogeneous distribution and inhibit aggregation. Finally, the solutions collected are poured into clean glass Petri dishes and oven-dried to extract excess solvent for two days at 50 °C. Films with a thickness of  $0.5 \pm 0.2$  mm were peeled from the dishes and kept in a vacuum desiccator.

### **2.2. Measurements**

Shimadzu Lab XRD-6000 diffractometer with  $\text{CuK}\alpha$  ( $= 1.5406 \text{ \AA}$ ) radiation at 30 kV voltage, 30 mA of the current used to measure X-ray diffraction patterns. Fourier transform infrared (FTIR) spectroscopy was carried out using a spectrophotometer Shimadzu, Model 8201 PC. This instrument measures in the wavenumber range 400–4000  $\text{cm}^{-1}$ . To measure the *ac* conductivity  $\sigma_{ac}$  and dielectric parameters, disk-shaped samples with radius 5 mm and thickness 0.5 mm were used. These disks were coated with silver paste and sandwiched between two polished brass electrodes. An automatic programmable RLC meter (FLUKE PM6306) was used to measure the capacitance  $C_p$ , in parallel and loss tangent ( $\tan\delta$ ) directly in the frequency range of 100 Hz - 1MHz and in the temperature range of 300 K - 390 K. The *ac* conductivity  $\sigma_{ac}$ , dielectric constant  $\epsilon'$  and dielectric loss  $\epsilon''$  were calculated for all investigated compositions according to the relations:

$$\epsilon'(\omega) = \frac{C_p t}{\epsilon_o A} \quad (1)$$

$$\epsilon'' = \epsilon' \tan\delta \quad (2)$$

where  $t$  is the sample thickness,  $A$  is its cross-section area, and  $\epsilon_o$  is the free space permittivity.

### **3. The proposed model; Artificial Neural Networks ANN model**

ANN simulates the way in which the human brains process information. ANN is a computational processing system that contains a large number of highly interconnected processing neurons. These neurons work together in a distributed manner to learn from data, coordinate internal processing, and optimize its final output. **Fig. 1** introduces the analogy between the biological and the artificial neurons. Each part in the biological neuron has an equivalent part and performs the same job in the artificial neuron. ANN network contains input layer, at least one hidden layer, and the outcome layer (See **Fig. 2**).

ANN have several benefits: the nature of adaptive learning from input information, using a suitable learning algorithm, and the ability to improve themselves. ANNs can learn and adapt through a training process. This empowers them to not only identify patterns in data but also generalize those patterns to solve similar problems. This makes them particularly valuable in applications like pattern recognition. Unlike traditional methods,

## Egypt J. Solids, Vol. (47) (2025)

ANNs can tackle complex, non-linear problems. They are also remarkably resilient, able to function effectively even with noisy or incomplete data, skillfully navigating around missing pieces of information. Despite the powerful capabilities of ANN model, it has some limitations. The reasoning behind their decisions remains opaque because of that adjusting weights is randomly performed based on the resulted errors. Furthermore, ANN depend on the size of experimental data. Overfitting is another prevalent issue, where the network performs well on training data but poorly on unseen data. But we can overcome the overfitting by selecting the optimal ANN architecture which avoid the excess of neurons. [27-30].

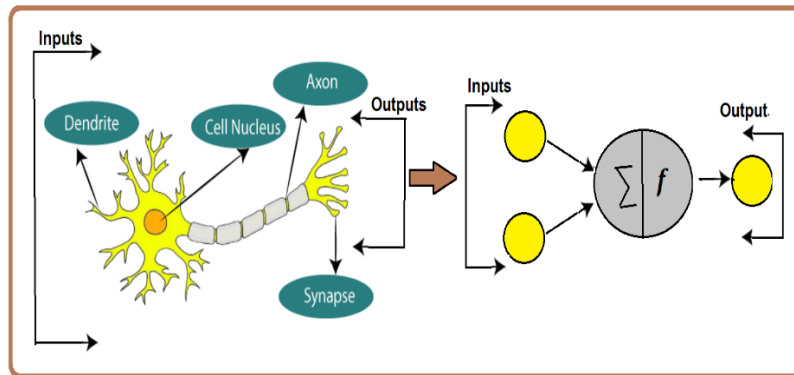


Fig.1: Analogy between the artificial neuron and biological neuron

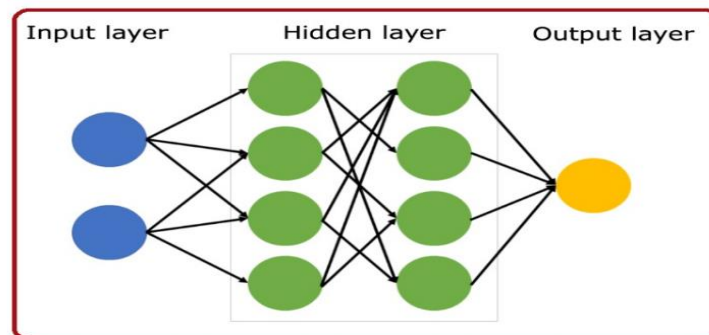


Fig.2: ANN structure

Backpropagation is a cornerstone calculating technique for utilizing ANNs. Its key strengths lie in its relative simplicity. Unlike other methods, it requires minimal parameter tuning beyond the initial inputs. Additionally, backpropagation exhibits impressive flexibility, readily adapting to different problems. However, it is crucial to acknowledge backpropagation's limitations. The noisy degree of the training datasets significantly impacts performance. Noisy data affects the algorithm performance. Despite these limitations, backpropagation remains effective for refining and testing ANN performance. There are certain procedures and mathematical equations for the backpropagation technique. The main procedures for training ANN include: entering the inputs, setting the ANN parameters, training the e data and calculating the error, checking whether it is

## R. A. Mohamed et al.

minimized or not and if the error is unacceptable, and updating the parameters (weights and biases). After that, the error is checked again. The process is repeated until the error becomes minimal. Once the error becomes minimal, you can feed some inputs to your model and it will produce the output. **Fig. 3** summarizes the steps of training ANN. Eq. (3) – (6) govern the ANN algorithm for n inputs.

The net input can be written in matrix form

$$n = wp + b \quad (3)$$

Where w is the weight, p is constant, and b is the bias.

The weights matrix w for m-neurons and N-layers case is given by:

$$\begin{bmatrix} W_{1,1} & W_{1,2} & W_{1,3} & \dots & \dots & W_{1,N} \\ W_{2,1} & W_{2,2} & W_{2,3} & \dots & \dots & W_{2,N} \\ W_{3,1} & W_{3,2} & W_{3,3} & \dots & \dots & \dots \\ \dots & \dots & \dots & \dots & \dots & \dots \\ \dots & \dots & \dots & \dots & \dots & \dots \\ W_{m,1} & W_{m,2} & W_{m,3} & \dots & \dots & W_{m,N} \end{bmatrix} \quad (4)$$

The layer output can be calculated using;

$$a_k = f_k(w_k p + b_k) \quad (5)$$

Where k is the layer number. It takes from 1 to N. The net output for S-neurons arranged in two layers can be computed by:

$$a_1 = f_1(w_1 p + b_1), \quad a_2 = f_2(w_2 a_1 + b_2) = f_2(w_2 f_1(w_1 p + b_1) + b_2) \quad (6)$$

Where  $a_1$  and  $a_2$  are the output of the first layer and second layer, respectively. [15]

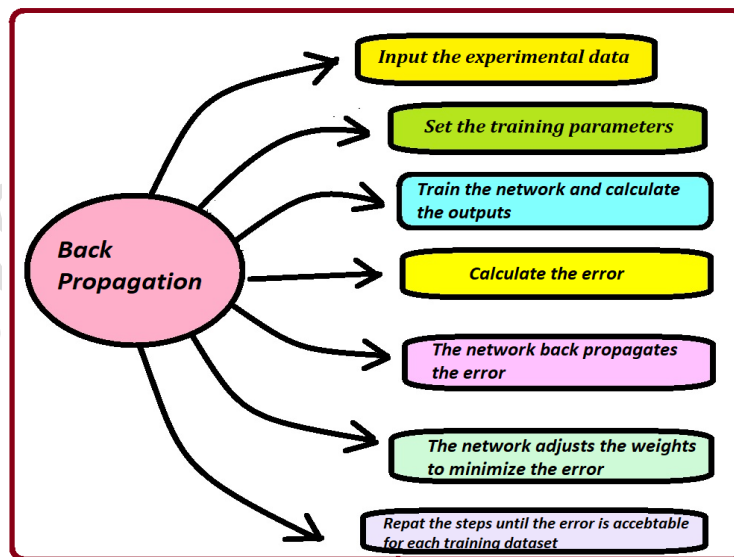


Fig.3: ANN back propagation procedures

## 4. Results and discussion

### 4.1. Structural analysis of PMMA/RGO nanocomposites

To investigate the changes in structural/crystalline properties of PMMA before and after RGO addition, XRD measurements were carried out. The XRD patterns of RGO NPs, neat PMMA and PMMA/RGO nanocomposites are depicted in **Fig. 4**. The XRD card number for PMMA is ICDD card No: 013-0835 and for rGO nanoparticles is JCPDS card No: 89-7213 and indexed the Miller indices values (002). The observed diffraction peak (002) in the XRD pattern of RGO NPs in its powder form was observed at  $2\theta = 25.5^\circ$  corresponding to the of interplanar distance about  $3.49 \text{ \AA}$  that is very consistent with that reported [31]. PMMA displays a broad peak at  $2\theta = 15.2^\circ$  which corresponds to the plane (111) with interplanar distance  $d = 5.824 \text{ \AA}$ . This peak reflects the ordered packing of polymer chains. Another weak peak centered at nearly  $31.2^\circ$  appeared with  $d = 2.864 \text{ \AA}$ , corresponding to the plane (112). The two wide humbs reflect PMMA's amorphous nature and are similar to previously reported  $2\theta$  values [32]. The addition of RGO NPs resulted in no significant movement in the locations of the amorphous humbs, but the humbs became larger with a lower intensity, indicating that such loading enhances PMMA's amorphicity [33]. Furthermore, there are no distinctive peaks for RGO NPs, indicating their solubility within the PMMA matrix. In other words, certain RGO NPs may deposit on free volume areas of the PMMA matrix.

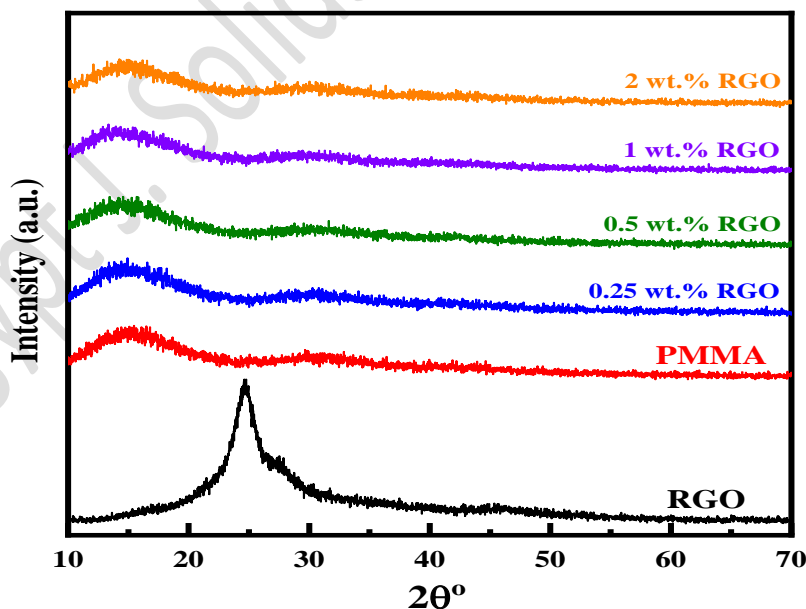


Fig. 4: XRD patterns of RGO, pure PMMA and PMMA/RGO nanocomposites doped with different contents of RGO NPs.

## **R. A. Mohamed et al.**

FTIR spectroscopy is well recognised as a valuable method for analysing structural information. Vibration bands provide insight into environmental changes and polymer structure at the molecular level. **Fig. 5** depicts the FTIR spectra of neat PMMA and PMMA doped with varying RGO concentrations. The films' spectra are very analogous, with just slight variations owing to RGO loading. This is because the examined materials are compatible, miscible, and create a homogeneous film. In other words, RGO NPs do not accumulate in the PMMA network. Absorbance bands in the 2800 to 3100  $\text{cm}^{-1}$  range, particularly at  $\sim 2965 \text{ cm}^{-1}$ , indicate C–H stretching of the methyl ( $\text{CH}_3$ ), ester-methyl, and methylene ( $\text{CH}_2$ ) groups [34]. The addition of RGO NPs reduces the strength of these bands and introduces two additional peaks at  $\sim 2957$  and  $2988 \text{ cm}^{-1}$ , corresponding to symmetric and asymmetric stretching of C–H. A minor peak at  $\sim 2843 \text{ cm}^{-1}$  corresponds to  $\text{CH}_2$  stretching vibration, which diminishes with RGO NPs loading. The distinctive peak at  $\sim 1749 \text{ cm}^{-1}$  is occurs because of the asymmetric stretching of the carbonyl group,  $\text{C}=\text{O}$ , of PMMA, which fits with previous published results [35].

Addition of RGO causes an increase in peak intensity. RGO addition also causes the tiny peak at  $\sim 1636 \text{ cm}^{-1}$  to move to  $\sim 1630 \text{ cm}^{-1}$ . This is known as the  $\text{C}=\text{C}$  stretching vibration. All films exhibit strong absorption bands below 1500  $\text{cm}^{-1}$ . The bands at 1350–1500  $\text{cm}^{-1}$  are mostly caused by different modes of C–H deformation. The peak at  $\sim 1348 \text{ cm}^{-1}$  is due to the methylene ( $-\text{CH}_2-$ ) group deformation mode, which vanished in a 2 wt.% RGO NPs doped film. Bands in the area  $\sim 1067$ – $1090 \text{ cm}^{-1}$  are attributed to the asymmetric stretching vibration of  $\text{C}-\text{O}-\text{C}$ . [36]. For the doped films, a sharp decrease in intensity was recorded. The bands at around 962–993  $\text{cm}^{-1}$  correspond to  $\text{C}-\text{C}$  stretching caused by  $\text{CH}_2$  bending and  $\text{O}-\text{CH}_3$  rocking mode. The peak at around 913  $\text{cm}^{-1}$  is known as  $=\text{CH}$  out of plane vibration. The peak at around 844  $\text{cm}^{-1}$  corresponds to the  $\text{CH}_2$  rocking mode. The band at  $\sim 810 \text{ cm}^{-1}$  corresponds to ester group vibrations, while the peak at  $\sim 752 \text{ cm}^{-1}$  represents  $\text{C}-\text{C}$  stretching [37]. The change in location and intensity of bands of pure PMMA is proof of the compatibility and interaction between RGO NPs and PMMA.

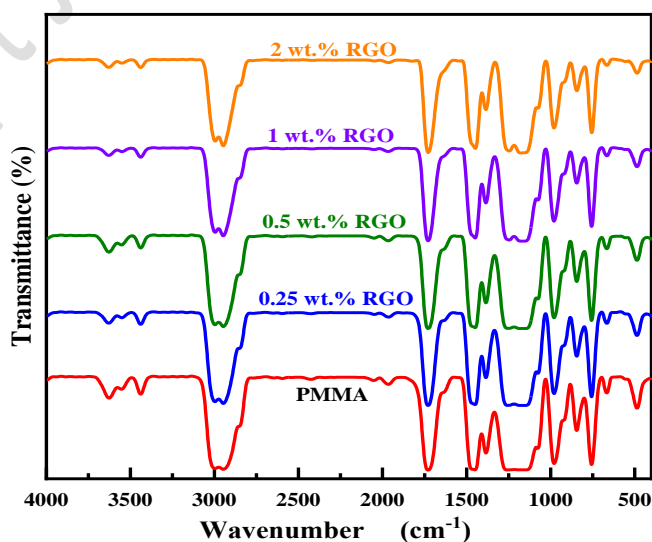


Fig.5: FTIR spectra of pure PMMA and PMMA/RGO nanocomposites doped with different contents of RGO NPs.

#### 4.2. Dielectric characterization of PMMA/RGO nanocomposites

Dielectric characteristics of PMMA/RGO polymer nanocomposites were examined in terms of frequency and temperature. The complex dielectric permittivity  $\epsilon^*$  of a system is defined as [38]:

$$\epsilon^* = \epsilon' - i \epsilon'' \quad (7)$$

where  $\epsilon'$  at low frequencies (100 Hz - 1 KHz), non-linear dispersion at medium frequencies (1 KHz - and  $\epsilon''$  are the real and imaginary parts of the dielectric constant, respectively.

**Fig. 6** shows the dependence of the dielectric constant  $\epsilon'$  on frequency for PMMA/RGO PNC films at different temperatures.  $\epsilon'$  is clearly frequency-dependent and drops as frequency increases. The  $\epsilon'$  spectra of these films across the examined frequency range (100 Hz - 1 MHz) exhibit three discrete zones of dispersion. High dispersion linear behavior is observed 20 KHz), and essentially steady-state behavior at high frequencies (20 KHz - 1 MHz). In the low frequency range of the spectra, dipoles that have enough time to align themselves under the applied field direction generate a significant reduction in  $\epsilon'$  with increasing frequency. This phenomenon, known as interfacial polarization or the Maxwell Wagner Sillars (MWS) effect, exists in materials constituted of two or more phases [39]. Interfacial polarization or Maxwell-Wagner-Sillars (MWS) polarization, occurs in heterogeneous systems, such as nanocomposite materials. MWS polarization arises from the accumulation of charges at the interface between two phases (PMMA and RGO) with different conductivity and dielectric properties. This interfacial charge accumulation leads to polarization by formation of electric dipoles at the interface and relaxation of these dipoles leading to a frequency-dependent dielectric response.

MWS effect mostly occurs in polymer nanocomposites PNC owing to the buildup or trapping of free charges at the filler polymer interfaces [40,41]. In the intermediate frequency region, the non-linear dispersion of  $\epsilon'$  spectra represent a mild polarization relaxation phenomenon with a progressive extinction of the interfacial polarization process in PNC films. As frequency increases, the dipole response is restricted and  $\epsilon'$  becomes saturated [42]. The micro-capacitor structure model leads to virtually constant steady-state behavior in the radio frequency band. [43]. Excess ions do not diffuse in the applied field direction, causing a drop in  $\epsilon'$  as frequency increases. As a result, charge carriers make a reduced contribution to the dielectric property [44]. At room temperature (RT = 300 K) the dielectric constant  $\epsilon'$  increases with increasing RGO content from ( $\epsilon' = 58$  at 1 KHz) for PMMA/0.25 wt.% RGO sample to ( $\epsilon' = 96$  at 1 KHz) for PMMA/2.0 wt.% RGO. The high conductivity of RGO NPs and their function in physical cross-linking arrangements in the PMMA matrix with increasing RGO concentration can explain the increase in  $\epsilon'$  [45]. This suggests that the addition of conductive nano-filler to the PMMA matrix promotes the creation of an RGO network inside the polymeric matrix, resulting in increased interfacial polarization. Higher dielectric constant ceramic particles absorb more charges as the

## **R. A. Mohamed et al.**

concentration of conducting RGO NPs in PNC films increases [46]. The interaction of RGO NPs with polymer chain segments promotes parallel dipolar alignments in functional groups, as evidenced by the dispersion behavior of  $\epsilon'$  values in PMMA/RGO films as filler concentration increases. As the filler concentration grows, so does the number of well-separated particles, which are responsible for the interaction between the filler and the polymer matrix, resulting in an increase in the dielectric constant. The observed increase in the dielectric constant  $\epsilon'$  with temperature for different concentrations of RGO may be attributed to formation of interface regions as an effect of reinforcement of RGO in between PMMA chains. Also, in this composite system, space charge polarization and thermal activation behavior come into picture due to movement of charge carriers trapped by interfaces leading to increased dielectric constant [45].

**Fig.7** shows the dependence of the dielectric loss  $\epsilon''$  on frequency PMMA/RGO PNC films. At low frequencies,  $\epsilon'$  values are consistently high. This behavior can be linked to the MWS effect, which allows charges to build at the interface of the sample and electrodes [47]. Because the carriers are unable to obey a particular applied field frequency,  $\epsilon''$  quickly diminishes as frequency increases. The polarisation of trapped carriers may be connected to this decline [48]. Additionally, it is noted that the observed rise in  $\epsilon''$  is caused by an increase in leakage current generated by the development of conductive channels in the PMMA matrix when the RGO volume percentage is increased. [49]. Electrical energy is transformed into thermal energy when an electrical field is provided because current flows via the conducting RGO NPs. At RT, the value of  $\epsilon''$  for PMMA/0.25 wt.% RGO sample at 1 KHz is 27 and increased to 59 for PMMA/2 wt.% RGO sample at 1 KHz, as shown in **Fig. 7**. Relaxation peak appears mainly in the intermediate frequency range and has major contribution to the dielectric losses. This relaxation peak arises from both  $\alpha$ -relaxation corresponding to the rotation of lateral groups of PMMA around its main chain axis and  $\beta$ -relaxation induced by the rotation of ester functional group ( $-\text{COOCH}_3$ ) around the C-C bond which link them to the main chain. [50]. This indicates that the synthesised PNCs have lower values of  $\epsilon''$  and a reasonably high  $\epsilon'$ , which are appropriate qualities for capacitor applications and can be employed as a dielectric medium in high energy storage capacitors. [51].

The dependence of both  $\epsilon'$  and  $\epsilon''$  on temperature for pure PMMA and PMMA/RGO PNC at fixed frequencies of 1 KHz and 1 MHz, as representative examples, are depicted in **Fig.8**. Due to thermal agitation, which improves the polar sites in the polymer chain's orientational freedom in accordance with the alternating field,  $\epsilon'$  rises with temperature for all tested samples [52]. As temperature rises to 360 K, dipoles become more responsive to the electric field, resulting in a progressive increase in  $\epsilon''$ . At higher temperatures ( $\geq 363$  K), the observed increment of  $\epsilon''$  values is due to a considerable increase in the RGO NPs doped PMMA matrix's interfacial polarization.

### **4.3. Ac conductivity**

The *ac* electrical conductivity  $\sigma_{ac}$  can be computed by the relation [53]:

$$\sigma_{ac} = \omega \varepsilon_0 \varepsilon' \tan \delta \quad (8)$$

Fig.9 shows the frequency dependence of  $\sigma_{ac}$  for pure PMMA and PMMA/RGO PNC at different temperatures. This figure shows that  $\sigma_{ac}$  grows with frequency for all examined

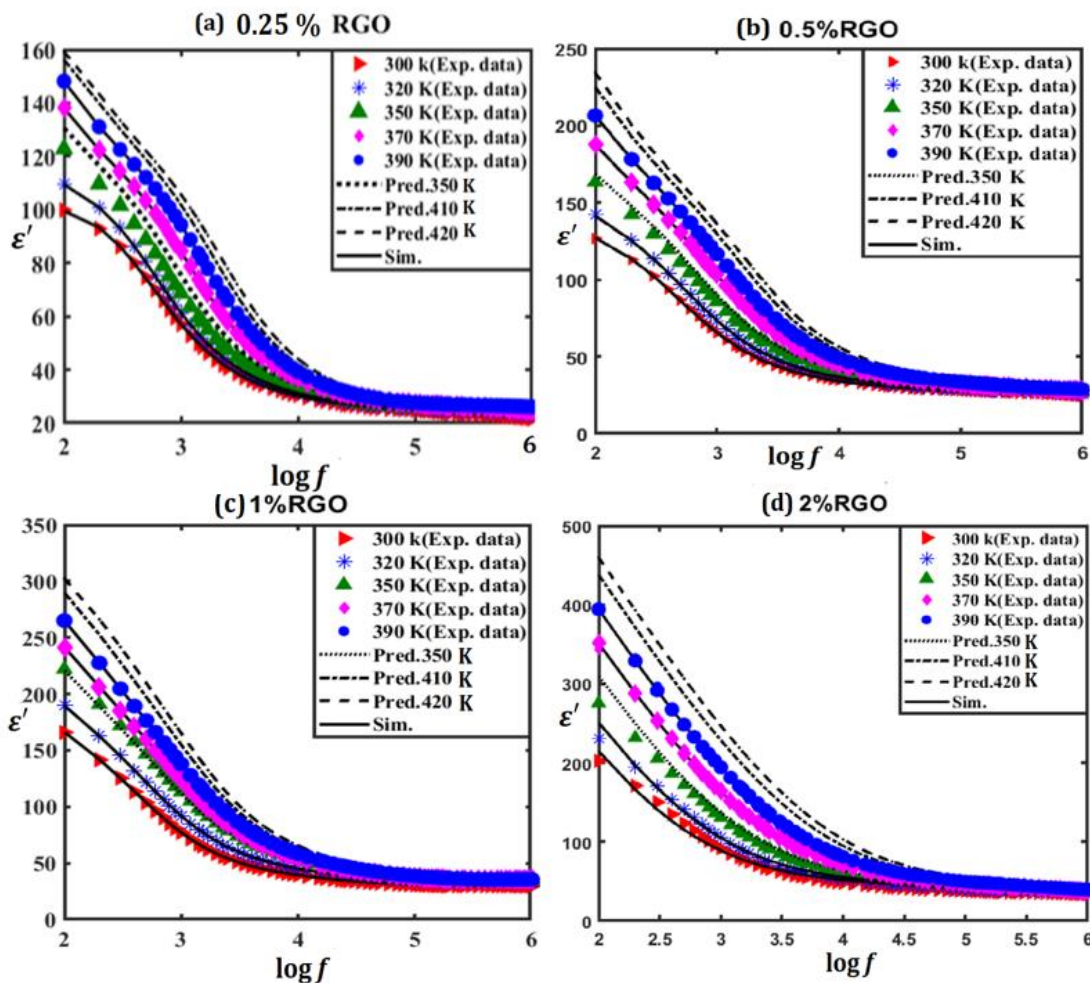


Fig 6: The ANN results of  $\varepsilon'$  against  $\log f$  at various  $T$  compared with their targets of various compositions of PMMA/RGO for ((a) 0.25% RGO, (b) 0.5% RGO, (c) 1% RGO, and (d) 2% RGO)

compositions, owing to rapid charge migration driven by increased absorbed energy. This energy causes charge accumulation, which increases the number of charge carriers due to the contribution of electronic polarization and the existence of free ions in the polymeric matrix. This behavior is typical of disordered materials under an electric field [54].

The electrical conductivity  $\sigma_{ac}$  of the investigated samples rises with increasing RGO concentration due to the creation of multiple conductive RGO pathways [50]. The  $ac$  electrical conductivity  $\sigma_{ac}$  at RT increased from  $6.35 \times 10^{-8} \Omega^{-1} \cdot \text{m}^{-1}$  for PMMA/0.25 wt.(%)

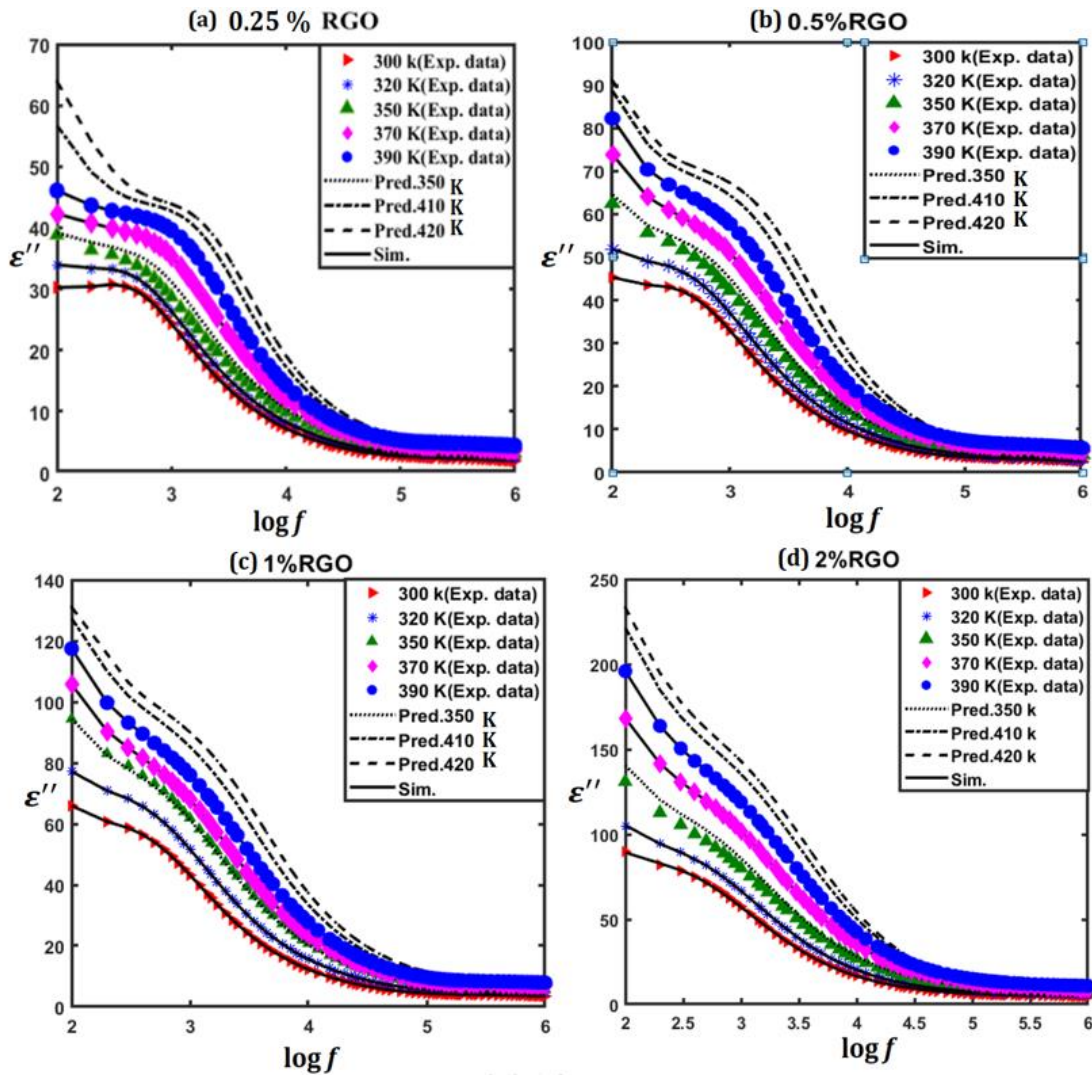


Fig 7: The trained ANN results (simulated and predicted) of  $\epsilon''$  vs.  $\log f$  compared with their targets at various  $T$  of PMMA/RGO with various compositions ((a) 0.25% RGO, (b) 0.5% RGO, (c) 1% RGO, and (d) 2% RGO)

RGO to  $4.58 \times 10^{-6} \Omega^{-1} \cdot \text{m}^{-1}$  for PMMA/2.0 wt.(%) RGO at 1 KHz. The rise in  $\sigma_{ac}$  with increasing RGO content is attributed to the large surface area and aspect ratio of RGO NPs, which leads to efficient charge transfer among the PMMA matrix and RGO nanoplatelets by bridging the separating gap and decreasing their potential barrier [55].

The  $ac$  conductivity  $\sigma_{ac}$  varies with the angular frequency  $\omega$  as [56]:

$$\sigma_{ac}(\omega) = A \omega^S \quad (9)$$

where  $A$  is constant depend on temperature and  $S$  is the frequency exponent. The most prevalent sort of conduction mechanism is determined by  $S$ 's temperature dependency. In the small polaron hypothesis,  $S$  grows with temperature, but in the big polaron theory,  $S$  initially falls and subsequently increases with temperature. In the correlated barrier hopping (CBH) model, the frequency exponent  $S$  decreases with increasing temperature

[57]. Based on Eq. (9), the values of  $S$  were calculated for all investigated samples from the slopes of the straight lines in the plots of  $\ln\sigma_{ac}$  versus  $\ln\omega$  in **Fig.9**. The obtained values of  $S$  are presented in **Table 1** for PMMA/RGO PNC films. The value of frequency exponent  $S$  depends upon temperature. By linear fitting of  $\ln\sigma_{ac}$  curves in Fig.9 in the medium and high frequency ranges, based on Eq. (9) the values of  $s$  parameter have been determined and tabulated in Table 1. for PMMA/RGO PNC films. The values of the exponent  $S$  decreased when the temperature increased, which can be described as a correlated barrier hopping (CBH) [58]. At higher temperature, the values of  $s$  parameter are low due to the thermal kinematics of mean free path of charge carriers i.e. increase in temperatures causes the liberation of more charge carriers thereby mediating the random thermal motion. Consequently, the average mean free path of charge carriers may be small due to successive more collision as compared to that at room temperature. This also signifies the transition of charge carrier mobility from long range to short range with rise in temperature.

According to the CBH model, conduction occurs when charge carriers hop between two localized locations and overcome their potential barrier. In this model, the following relationship can express the  $ac$  conductivity  $\sigma_{ac}$  [59,60]:

$$\sigma_{ac}(\omega) = \frac{\pi^3}{3} N^2 \varepsilon'(\omega) \varepsilon_o \omega R_\omega^6 \quad (10)$$

where  $N = k_B T N(E_F)$  is the site pairs concentration,  $N(E_F)$  is the density of states at the Fermi level. The exponent  $S$  is given by:

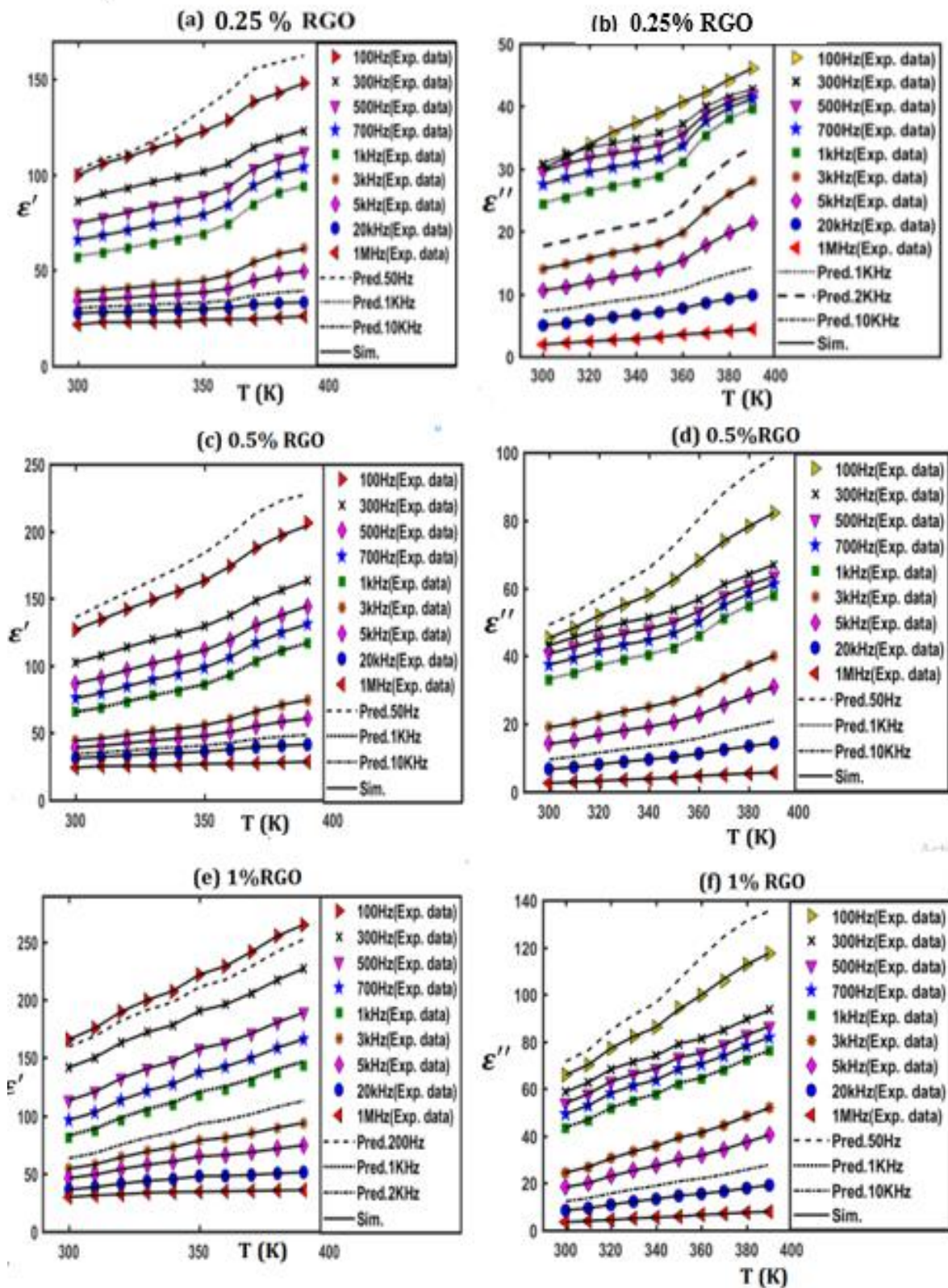
$$S = 1 - \frac{6 k_B T}{W_m + k_B T \ln(\omega\tau_o)} \quad (11)$$

where  $W_m$  is the maximum barrier height or the binding energy,  $R_\omega$  is the hopping distance and  $\tau_o$  is the characteristic relaxation time ( $\tau_o = 10^{-12}$  s) [61]. Using the approximation  $\ln(\omega\tau) < W_m$ , Eq. (10) becomes:

$$S = 1 - \frac{6 k_B T}{W_m} \quad (12)$$

The charge carriers binding energy  $W_m$  can be calculated from Eq. (8) by substituting with the corresponding values of the frequency exponent  $S$ . The calculated values of  $W_m$  for PMMA/RGO PNC at fixed temperatures are listed in **Table 1**. It is obvious that,  $W_m$  decreases with both temperature and RGO content which can be discussed by Pike model [62]. The overlapping of adjacent site's potential wells lowers the effective barrier height from  $W_m$  to the hopping barrier height  $W_H$  and verifies the condition  $W_H/W_m < 0.5$ . When a strong overlapping between potential wells occurs, the  $W_H \approx W_m/4$ . Therefore, the decrement of  $W_m$  with temperature may be due to the increment of the overlapping between potential wells within the matrix.

The variation of  $\ln\sigma_{ac}$  with temperature for pure PMMA and PMMA/RGO PNC films at different frequencies is shown in **Fig. 10**. This figure shows that  $\sigma_{ac}$  for the tested film



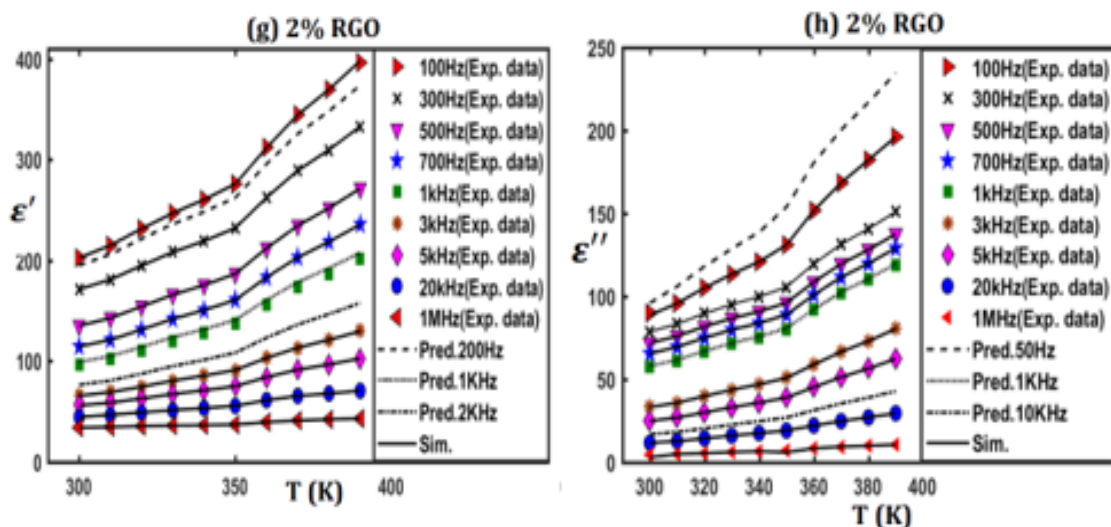
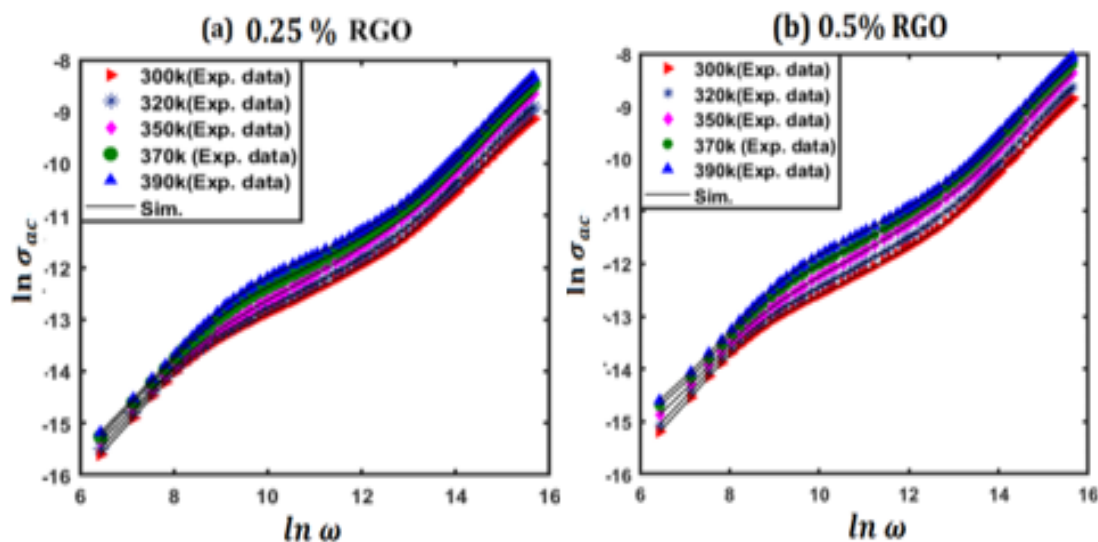


Fig 8: Temperature dependence of both  $\epsilon'$  and  $\epsilon''$  at various  $f$  of PMMA/RGO for various compositions ((a), (b) 0.25% RGO), ((c), (d) 0.5% RGO), ((e), (f) for 1% RGO), and ((g), (h) for 2% RGO)), respectively.

samples grows non-linearly with temperature, and the change is more significant at higher temperatures. This implies that  $\sigma_{ac}$  is a thermally triggered process from different localised states in the bandgap [63]. When the temperature rises, the polymer chains have an easy path to shift segments that offer ion migration channels, leading to an increase in ac conductivity  $\sigma_{ac}$ . The activation energy values are calculated for the investigated samples at a frequency 10 KHz as representative example and the data are listed in **Table 1**.



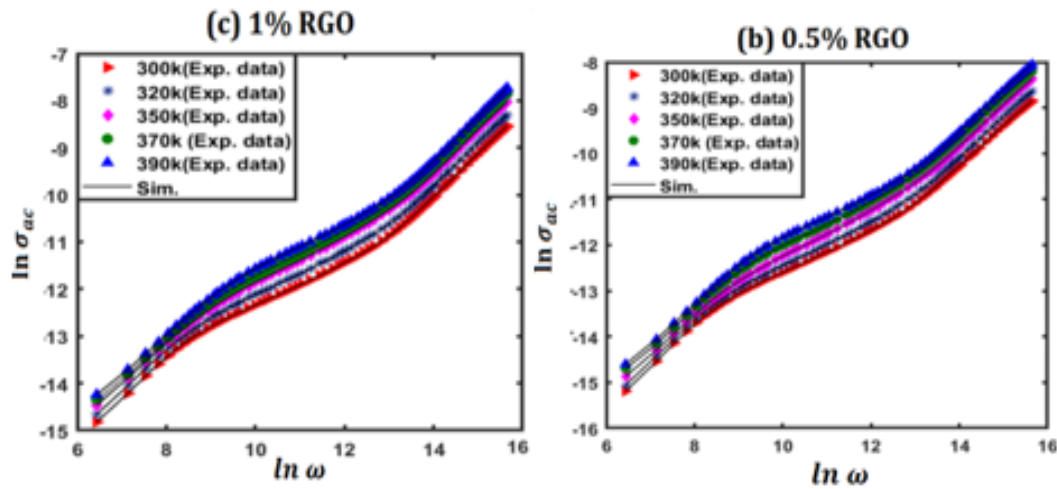


Fig 9: Comparison between the practical results and ANN modeling outputs of the frequency dependence of  $\ln \sigma_{ac}$  at various  $T$  of PMMA/RGO with various compositions ((a) 0.25% RGO, (b) 0.5% RGO, (c) 1% RGO, and (d) 2% RGO)

It is noticed that the activation energy  $E_a$  decreases with increasing RGO content indicating that the increment of the RGO percentage facilitates the charge carriers jumping between localized states. The smaller values of the activation energy and enhancing the conductivity with rising RGO concentration confirm that the conduction is governed by the hopping mechanism [63].

#### 4.4. ANN modeling results

ANN is utilized in modeling the ac conductivity and dielectric properties of PMMA/RGO polymer. The main aim is to select the best ANN configuration capable of simulating the experimental data and predicting unmeasured values with high precision and minimum error rates. The training was processed based on MATLAB (R2018a). The experimental data are presented as inputs in the ANN model. 6 networks were trained to model 24 datasets containing about 100 data points for each dataset. Each dataset consists of two inputs and corresponding one target output. Different ANN configurations were trained to determine the optimum network. This technique has been achieved by adjusting the number of hidden neurons, the number of hidden layers, the transfer function, and the training algorithm to achieve the best ANN performance. The parameters and characteristics relevant to the optimum ANN network are recorded in **Table 2**. The values of the regression coefficient (R) and mean square error (MSE) were calculated. The mean squared error MSE function was calculated to determine the ANN accuracy. The values of R, as well as MSE, were the indicators to select the best ANN structure. R and MSE values were computed based on Eq. (14), (15). [19], [20]

$$e = (pred - exp) \quad (13)$$

$$R = \sqrt{\left(1 - \frac{\sum_{t=1}^n e^2}{\sum_{t=1}^n (exp - \overline{exp})^2}\right)} \quad (14)$$

$$MSE = \frac{1}{n} \sum_{t=1}^n e^2 \quad (15)$$

During the learning process adjusting weights based on the back-propagation technique is the essential step to reach the best performance. It is noted that the symbols, solid, and dashed curves represent the experimental data, ANN simulated results, and ANN predicted results, respectively. Consider **Fig. 6**, it presents ANN training results for  $\epsilon'$  and frequency as  $\log f$  at different temperatures and compositions 0.25%, 0.5%, 1%, and 2%. Analyzing **Fig. 6**, the simulated solid curves and the symbols of the experimental data closely match, demonstrating the accuracy of ANN results. 2 kinds of predictions are performed. Prediction of experimentally measured values at 350 k. A second set of predictions were processed at 410k and 420k showing acceptable results. The ANN training results follow the experimental data patterns and provide acceptable error rates. ANN outputs of  $\epsilon''$  are introduced in **Fig.7** which demonstrates that the simulation results exactly follow the experimental data patterns. Predictions of experimentally measured  $\epsilon''$  are processed at temperature 350k while the predictions of experimentally unmeasured  $\epsilon''$  are performed at 410k and 420k. Predictions are performed for the compositions understudy. Prediction results are compatible with the experimental measurements. **Figs. 8** represent the ANN modeling results for  $\epsilon'$  and  $\epsilon''$  as a function of temperature for thickness at different frequencies and compositions. According to **Figs. 8**, ANN simulation results introduce a very good agreement with the experimental data. Predictions as testing steps are processed at 1 KHz. While predictions for unmeasured values are processed for (200Hz, 2 KHz) and (50Hz, 10 KHz) for  $\epsilon'$  and  $\epsilon''$ , respectively. The prediction results prove the excellent ability and great efficiency of the ANN. **Fig. 9** showed ANN simulation results and experimental data of  $\ln\sigma_{ac}$  vs.  $\ln\omega$  for different temperatures and compositions. A simulation process was carried out and compared with the experimental data showing great agreement and provide very good accordance. Consider **Fig. 10** shows the ANN outputs of  $\ln\sigma_{ac}$  vs.  $1000/T$  for different frequencies and compositions. It noted that ANN simulation output and their targets behave similarly. Predictions of experimentally measured values are performed for at 300 Hz. Predictions for unmeasured values are performed at 50Hz and 2MHz for all compositions. Prediction outputs demonstrate ANN excellent performance and excellent efficiency. A clear evidence of ANN accuracy is introduced by calculating the mean squared MSE for all trained parameters. MSE values for the trained parameters are recorded in **Table 3**. Analyzing **Table 3**, it noted that MSE values are very small ( $10^{-10} < MSE < 0.08$ ) which express the compatibility and great matching between modeling outputs and their targets for the trained datasets. The MSE values relevant to **Fig. 8** and **Fig.10** are plotted and introduced in **Fig. 11 (a-h)** and **Fig. 12 (a-d)**, respectively. The regression coefficient R is a valuable tool for evaluating how well ANN model

### **R. A. Mohamed et al.**

captures the relationship between variables, but it should be used in conjunction with other error functions like MSE for a more comprehensive assessment of model performance. R has a value between 0 and 1. A higher R value indicates more fitting. An R value of 1 represents a perfect fit, where the model perfectly predicts the dependent variable. **Fig. 13 (a)-(d), Fig. 14 (a)-(d)** represent the regression coefficient R of ANN model relevant to **Fig. 8** and **Fig.10**. R values showed the closeness and complete agreement between ANN outputs and input. It is important to mention that associated MSE and R values are calculated and plotted for all trained variables. **Figs 11 – 14** were displayed as an example. The remaining figures were deleted to prevent elongation and repetition.

**Table 1: Values of frequency exponent  $S$  , charge carriers binding energy  $W_m$  and activation energy  $E_a$  for PMMA/RGO nanocomposites.**

Sample	$S$				$W_m$ , eV				$E_a$ , eV at $f = 10\text{KHz}$
	300K	330K	360K	390K	300K	330K	360K	390K	
<b>0.25</b>	0.913	0.861	0.729	0.587	1.095	0.973	0.665	0.512	0.2864
<b>0.50 wt.%</b>	0.892	0.850	0.718	0.568	1.025	0.926	0.648	0.494	0.2327
<b>1 wt.%</b>	0.887	0.838	0.675	0.502	0.998	0.88	0.578	0.441	0.1862
<b>2 wt.%</b>	0.881	0.826	0.651	0.482	0.965	0.835	0.546	0.427	0.1673

**Table 2: Configuration of the optimum ANN network**

Training Parameter	Values
Neural network model	Back Propagation
Datasets	24
Dataset points	2400
Input nodes	2
Hidden layer	2
Hidden layers neurons	10
Output nodes	1
Output layer neurons	1
Transfer function of hidden layers	Log-sigmoid
Transfer function of output layer	Pure-line
No. of epochs	1000
Performance	Mean squared error MSE

Table 3: Mean Squared Errors MSE values of the trained ANN networks

The trained parameters	MSE			
	0.25 wt. % RGO	0.5 wt. % RGO	1 wt. % RGO	2 wt. % RGO
$\varepsilon'$ vs $\log f$	$8.7 \times 10^{-6}$	$9.6 \times 10^{-6}$	$9.9 \times 10^{-6}$	$9.56 \times 10^{-6}$
$\varepsilon''$ vs $\log f$	0.022969	0.024564	0.056277	0.089441
$\varepsilon'$ vs $T$	$2.5 \times 10^{-6}$	$3 \times 10^{-6}$	$9.9 \times 10^{-5}$	$5 \times 10^{-5}$
$\varepsilon''$ vs $T$	$5.9 \times 10^{-8}$	$4 \times 10^{-5}$	$1.6 \times 10^{-6}$	$1.7 \times 10^{-4}$
$\ln \sigma_{ac}$ vs. $\ln \omega$	$1.5 \times 10^{-3}$	$2.2 \times 10^{-3}$	$4.5 \times 10^{-3}$	$8.9 \times 10^{-3}$
$\ln \sigma_{ac}$ vs. $1000/T$	$9.4 \times 10^{-6}$	$2 \times 10^{-5}$	$4.7 \times 10^{-6}$	$1.35 \times 10^{-10}$

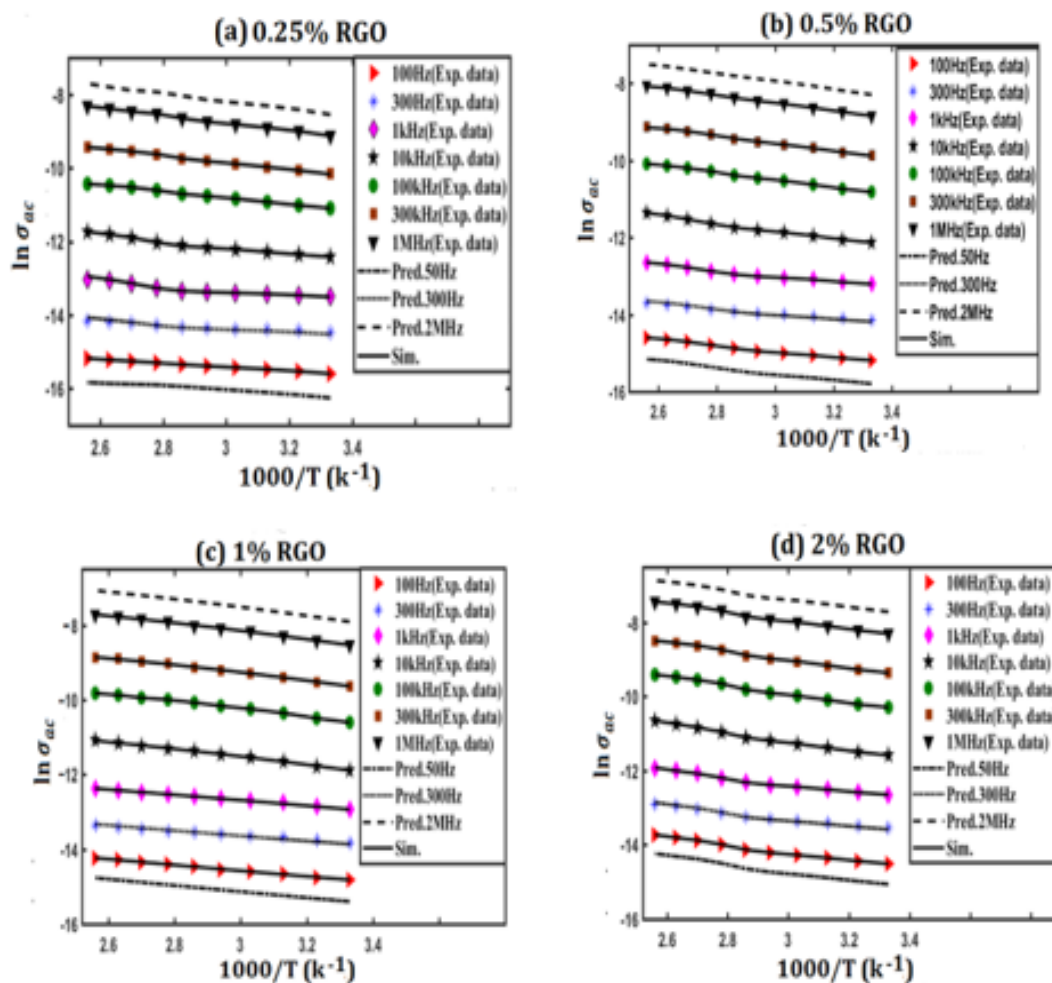


Fig 10: Comparison between the practical results and ANN modeling outputs of  $T$  dependence of  $\ln \sigma_{ac}$  at various  $f$  of PMMA/RGO with various compositions ((a) 0.25% RGO, (b) 0.5% RGO, (c) 1% RGO, and (d) 2% RGO)

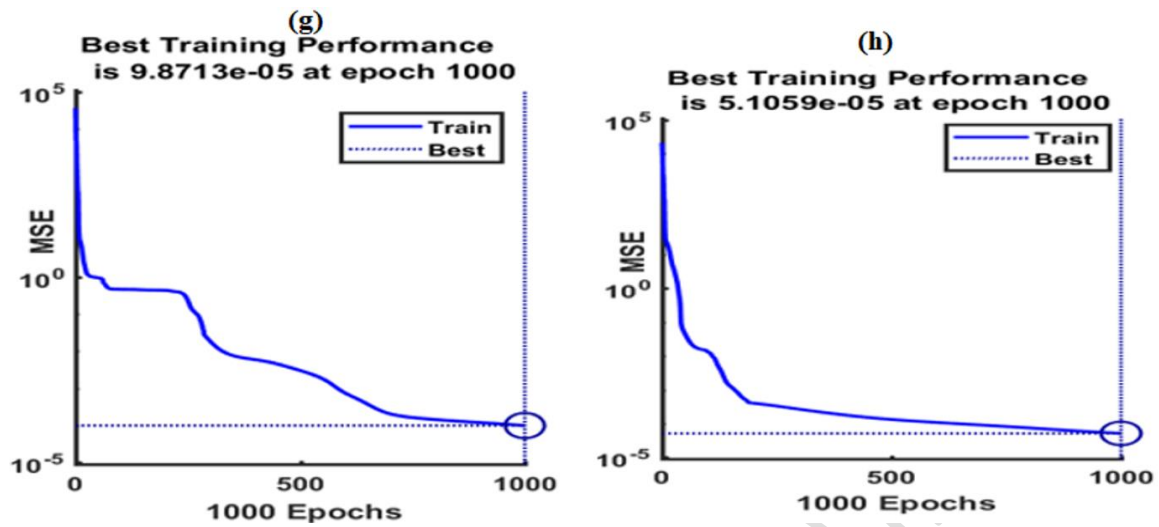
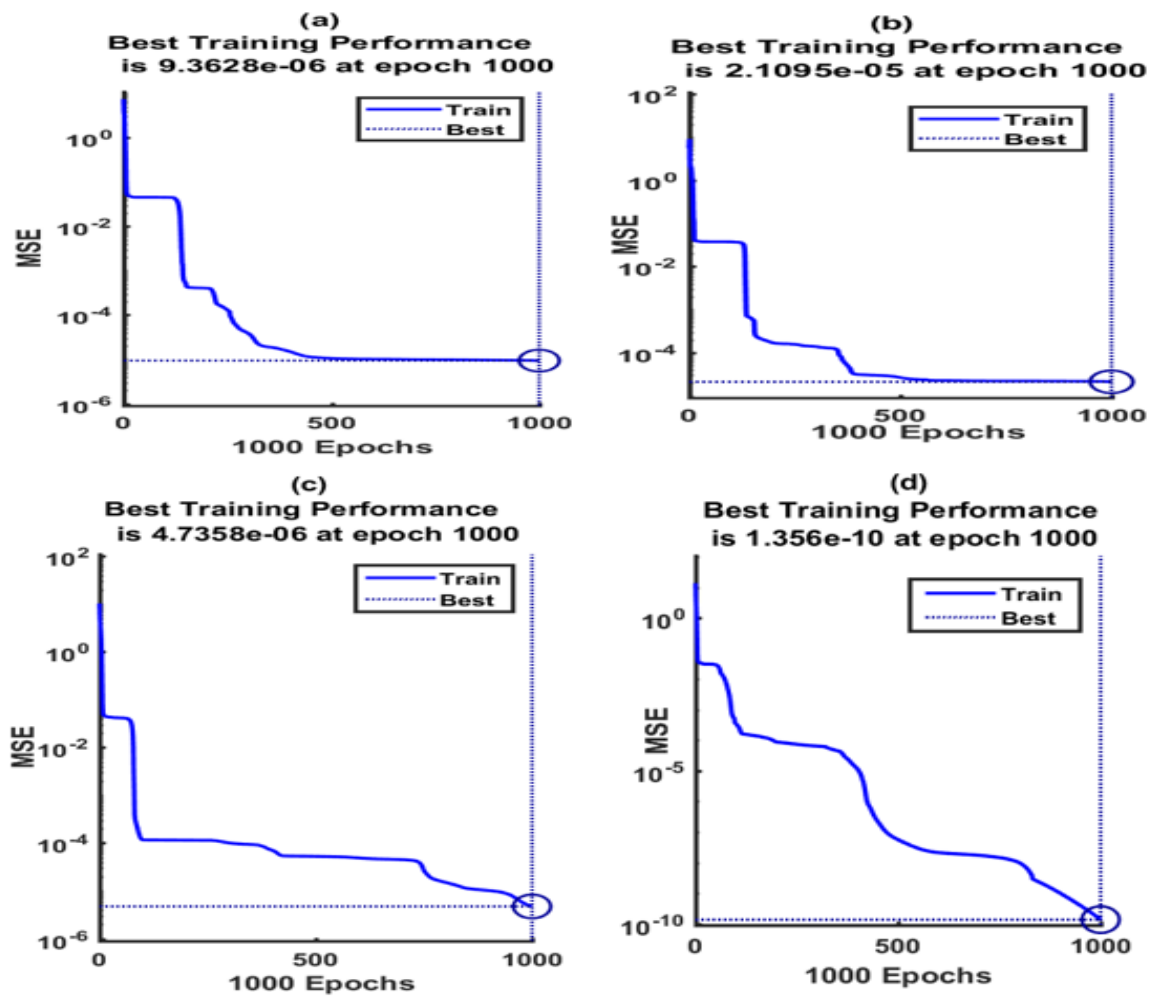


Fig 11: ANN performance relevant to Fig. 8



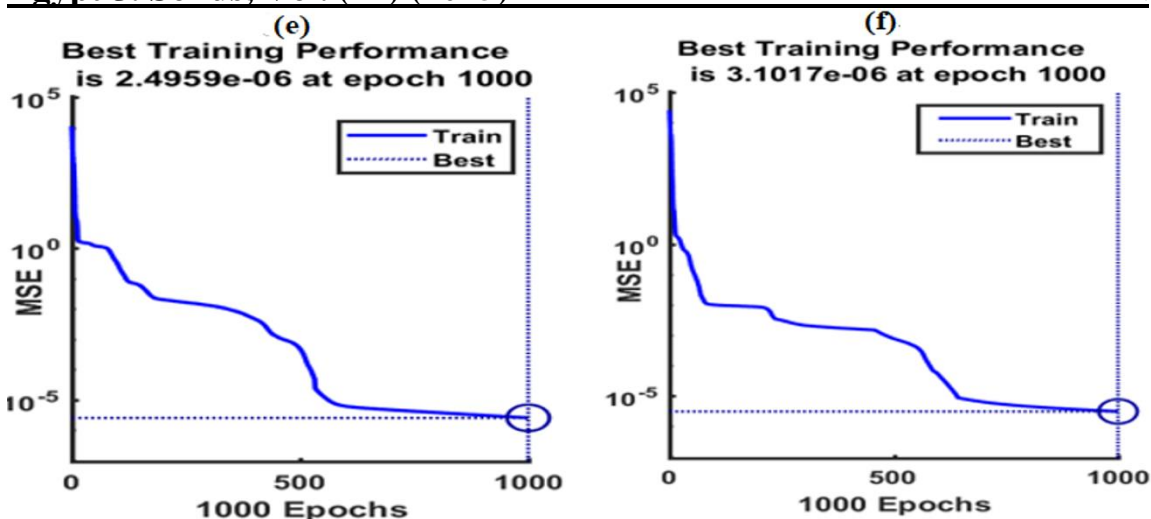
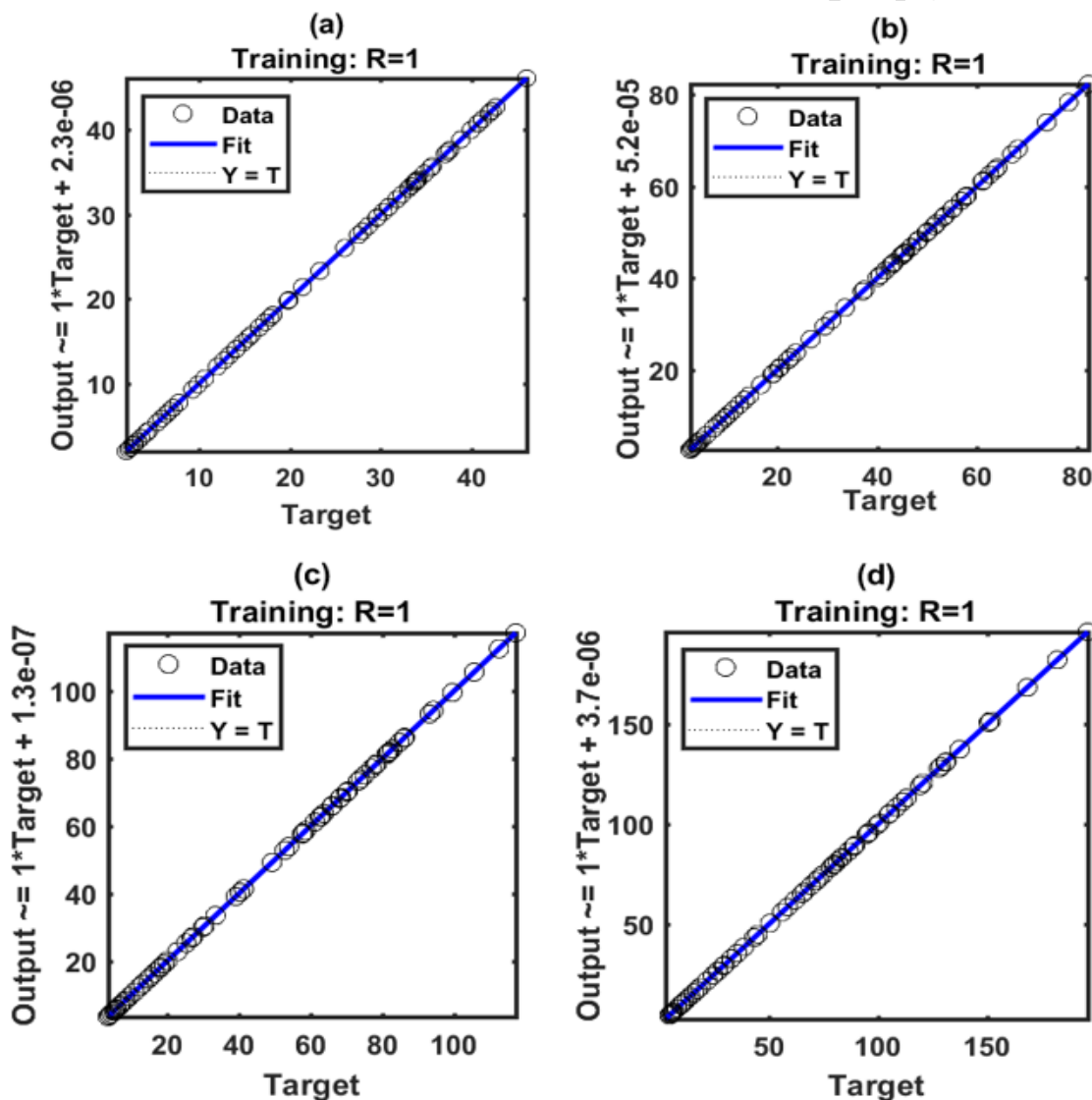


Fig. 12: ANN performance relevant to Fig. 10



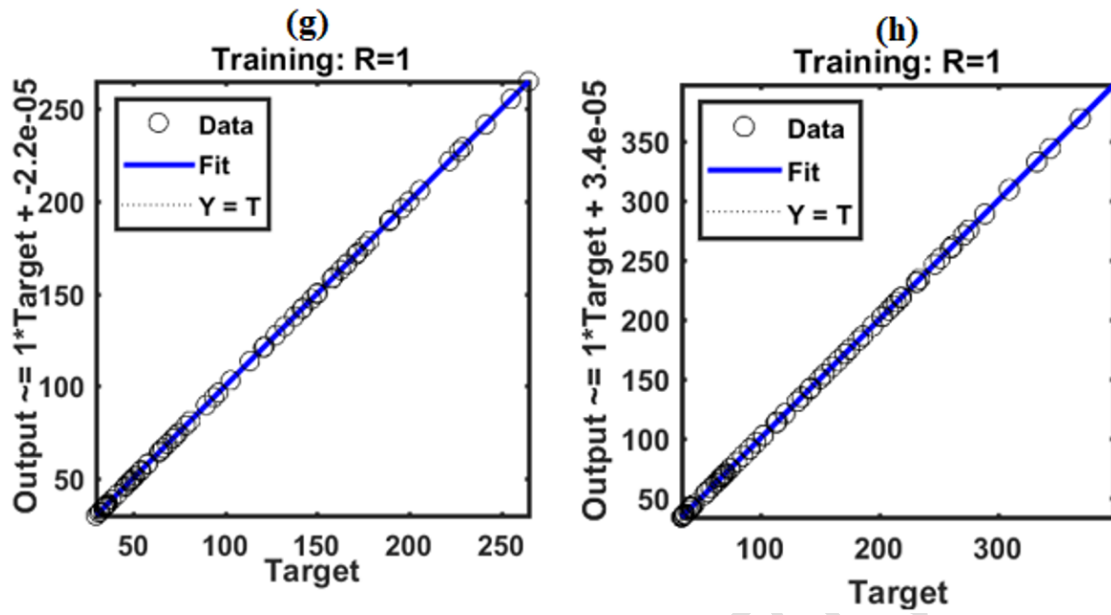
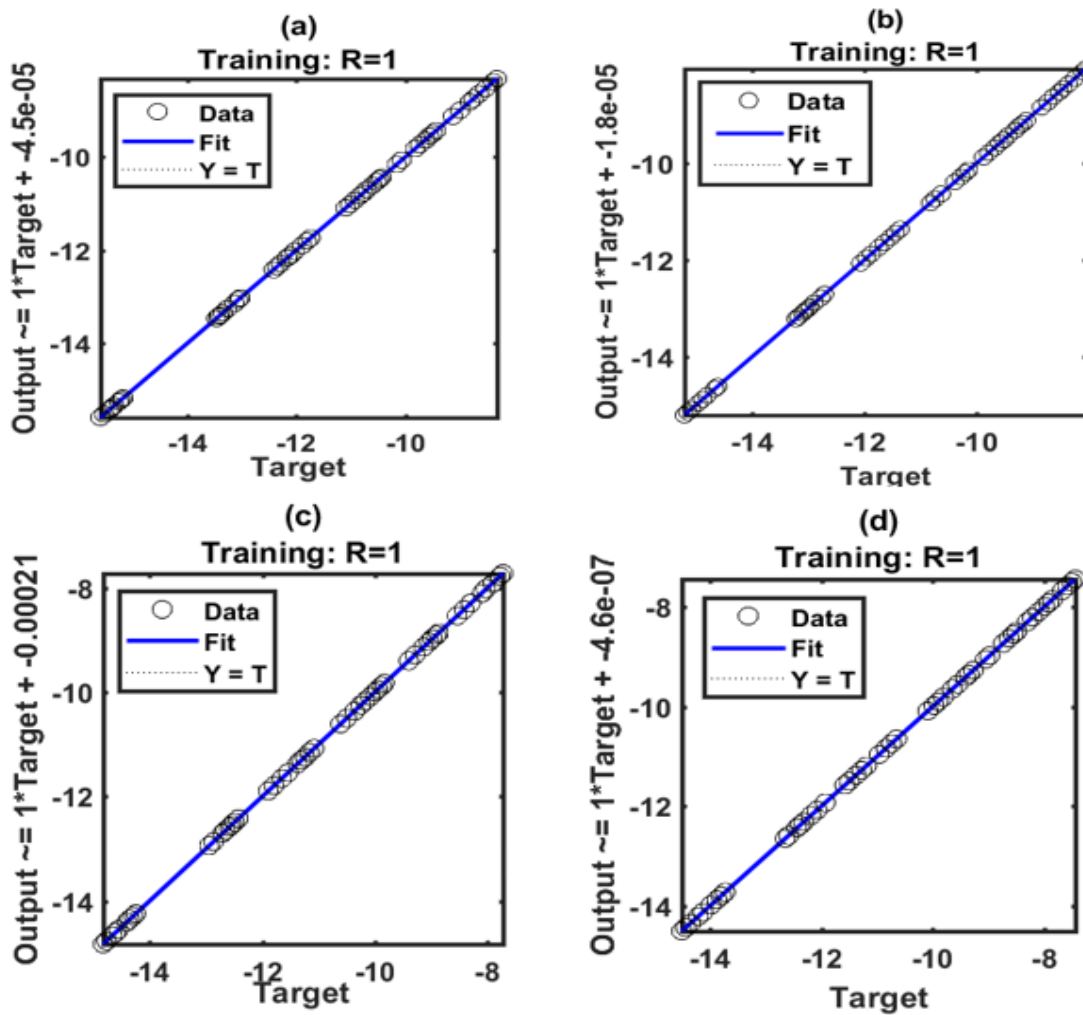
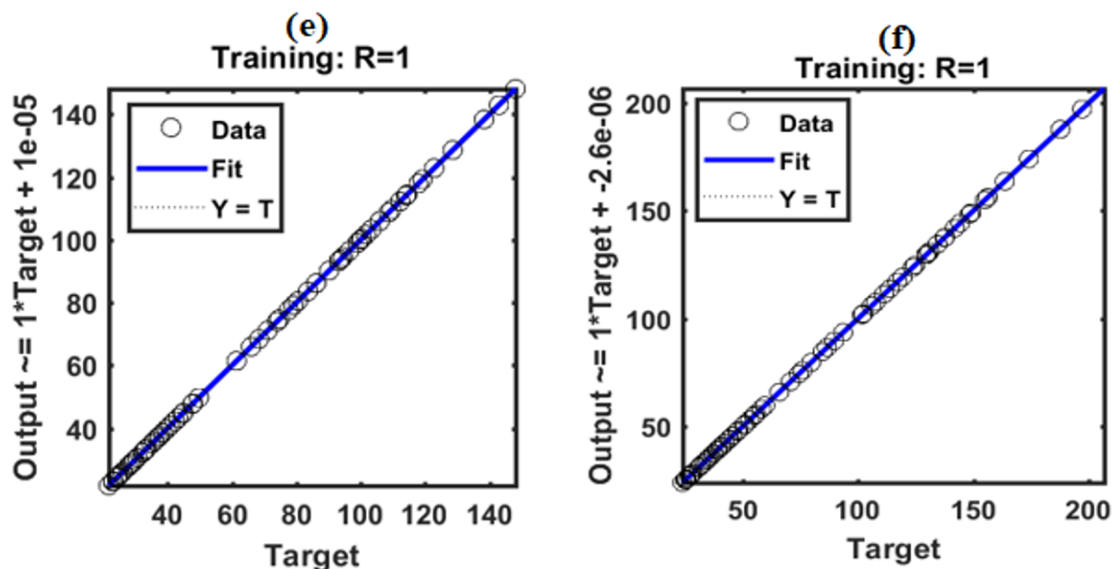


Fig. 13: Regression coefficient relevant to the training of ANN relevant to Fig. 8





**Fig. 14: Regression coefficient relevant to the training of ANN relevant to Fig. 10**

#### Conclusion:

This research investigates the dielectric behavior of PMMA/RGO nanocomposites through an integrated experimental and theoretical approach. The dielectric constant, loss tangent, and AC conductivity were found to be strongly dependent on both frequency and temperature. The incorporation of RGO nanoparticles as dopants significantly enhanced these electrical properties, making the nanocomposites promising candidates for various electronic applications. Furthermore, an artificial neural network ANN model effectively simulate and predict the dielectric behavior of the nanocomposites. The trained ANN achieved excellent agreement with the experimental data, as evidenced by minimal mean squared errors MSE and regression coefficient R values. This demonstrates the capability of ANN as a powerful tool for understanding and predicting the complex dielectric behavior of polymer nanocomposites. The obtained numerical ANN equations offer valuable tools for future research and development in this field. Overall, this study highlights the potential of RGO-doped PMMA nanocomposites for electronic applications and demonstrates the effectiveness of ANN in modeling their dielectric behavior.

#### Declaration of Conflicting Interests

The authors declared no potential conflicts of interest concerning the publication of this article.

Data availability: Data will be made available on request.

**R. A. Mohamed et al.****References:**

- 1- A. M. El Sayed, Aspects of structural, optical properties, and relaxation in (BiFeO<sub>3</sub> or NaTiO<sub>3</sub>)–PMMA: Hybrid films for dielectric applications, *Journal of Physics and Chemistry of Solids*, 148 (2021) 109767.  
<https://doi.org/10.1016/j.jpcs.2020.109767>
- 2- M.M. Abutalib, Insights into the structural, optical, thermal, dielectric, and electrical properties of PMMA/PANI loaded with graphene oxide nanoparticles, *Physica B* 552 (2019) 19–29.  
<https://doi.org/10.1016/j.physb.2018.09.034>
- 3- E. A. Stefanescu, X. Tan, Z. Lin, N. Bowler, M. R. Kessler, Multifunctional fiberglass-reinforced PMMA-BaTiO<sub>3</sub> structural/dielectric composites, *Polymer*, 52 (2011) 2016–2024.  
<https://doi.org/10.1016/j.polymer.2011.02.050>
- 4- W. Liu, Z. Xie, Y. Lu, M. Gao, W. Zhang, L. Gao, Fabrication and excellent electroresponsive properties of ideal PMMA@BaTiO<sub>3</sub> composite particles, *RSC Adv*, 9 (2019) 12404–12414.  
<https://doi.org/10.1039/C9RA01174A>
- 5- C.M.S. Prasanna, A. Suthanthiraraj, Electrical, structural, and morphological studies of honeycomb-like microporous zinc-ion conducting poly (vinyl chloride)/poly (ethyl methacrylate) blend-based polymer electrolytes, *Ionics*, 22 (2016) 389–404.  
<https://doi.org/10.1007/s11581-015-1546-4>
- 6- P. Maji, R. B. Choudhary, M. Majhi, Structural, electrical and optical properties of silane-modified ZnO reinforced PMMA matrix and its catalytic activities, *Journal of Non-Crystalline Solids*. 456 (2017) 40–48.  
<https://doi.org/10.1016/j.jnoncrysol.2016.10.039>
- 7- C.G. Alvarado-Beltrán, J.L. Almaral-Sánchez, R. Ramírez-Bon, Synthesis and properties of PMMA-ZrO<sub>2</sub> organic–inorganic hybrid films, *J. Appl. Polym. Sci*, 132 (2015), 42738.  
<https://doi.org/10.1002/app.42738>
- 8- A.M. Ismail, M.I. Mohammed, S.S. Fouad, Optical and structural properties of polyvinylidene fluoride (PVDF) / reduced graphene oxide (RGO) nanocomposites, *Journal of Molecular Structure* 1170 (2018) 51–59.  
<https://doi.org/10.1016/j.molstruc.2018.05.083>
- 9- L. Noein , M. Razzaghi-Kashani, The effects of interfacial layers on dielectric properties of an acrylic co-polymer containing polymer-grafted reduced graphene oxide, *Colloids and Surfaces A: Physicochemical and Engineering Aspects* 688 (2024) 133650.  
<https://doi.org/10.1016/j.colsurfa.2024.133650>
- 10- R. A. Althobiti, M. A. Morsi, E. Alzahrani, A.A. Al-Muntaser, Enhancing the performance of PVC/PMMA polymer blend through hybrid nanofiller of TiO<sub>2</sub>

- NPs/GNPs for capacitive energy storage applications, *Ceramics International* 50 (2024) 19039–19047.  
<https://doi.org/10.1016/j.ceramint.2024.03.001>
- 11- R.A. Mohamed, Application of Artificial Neural Network Model for Prediction of Thermo-Physical Properties of Carbon Nanotubes (CNTs) Containing Nanofluid, *Nanofluids* 8 (2019) 1–6.  
<https://doi.org/10.1166/jon.2019.1573>
- 12- Z Zhang, K Friedrich, Artificial neural networks applied to polymer composites: a review, *Composites Science and Technology*, 63(2003) 2029-2044  
[https://doi.org/10.1016/S0266-3538\(03\)00106-4](https://doi.org/10.1016/S0266-3538(03)00106-4)
- 13- K Friedrich, K. Nasri, L. Toubal, Artificial Neural Network Approach for Assessing Mechanical Properties and Impact Performance of Natural-Fiber Composites Exposed to UV Radiation, *Polymers* 16(2024) 538.  
<https://doi.org/10.3390/polym16040538>
- 14- I. Khasanshin, Application of an Artificial Neural Network to Automate the Measurement of Kinematic Characteristics of Punches in Boxing, *Appl. Sci.* 11(2021) 1223.  
<https://doi.org/10.3390/app11031223>
- 15- H.A.M. Ali, R.A. Mohamed, Modeling for electrical impedance spectroscopy of (4E)-2-amino-3-cyanobenzo[b]oxocin-6-one by artificial neural network, *Ceramics International* 44 (2018) 10907–10911  
<https://doi.org/10.1016/j.ceramint.2018.03.146>
- 16- E. Champa-Bujaico, P. García-Díaz, A. M. Díez-Pascual, Machine Learning for Property Prediction and Optimization of Polymeric Nanocomposites, *Int. J. Mol. Sci.* 23(2022) 10712  
<https://doi.org/10.3390/ijms231810712>
- 17- J.N. Kumar, Q. Li, Y. Jun, Challenges and opportunities of polymer design with machine learning and high throughput experimentation, *Artificial Intelligence Prospective*, 9(2) (2019) 537–544  
<https://doi.org/10.1557/mrc.2019.54>
- 18- W. Sha, Y. Li, S. Tang, J. Tian, Y. Zhao, Y. Guo, W. Zhang, X. Zhang, S. Lu, Y. Cao, S. Cheng, Machine learning in polymer informatics, *InfoMat.* 3(4) (2021) 353–361  
<https://doi.org/10.1002/inf2.12167>
- 19- R. A. Mohamed, H.E. Atyia, Predicting the AC conductivity of semiconductor composition thin films using ANFIS model; an integrated experimental and theoretical approach, *Phys. Scr.* 99 (2024) 046004  
<https://doi.org/10.1088/1402-4896/ad301e>
- 20- R. A. Mohamed, H.E. Atyia, Comparative analysis of machine learning techniques in predicting dielectric behavior of ternary chalcogenide thin films, *Phys. Scr.* 99 (2024) 126003  
<https://doi.org/10.1088/1402-4896/ad86f9>

**R. A. Mohamed et al.**

- 21- H. Li, X. Liu, S. Yang, Z. Yang T. Yi, W. Yuan, Prediction of Polarizability and Absolute Permittivity Values for Hydrocarbon Compounds Using Artificial Neural Networks, *Int. J. Electrochem. Sci.* 9 (2014) 3725–3735.  
[https://doi.org/10.1016/S1452-3981\(23\)08045-8](https://doi.org/10.1016/S1452-3981(23)08045-8)
- 22- N.V. Artemenko, I.I. Baskin, V.A. Palyulin, N.S. Zefirov, Artificial neural network and fragmental approach in prediction of physicochemical properties of organic compounds, *Russ. Chem. Bull.* 52 (1) (2003) 20.  
<https://doi.org/10.1023/A:1022467508832>
- 23- Z. Shahryari, A. Sharifi, A Mohebbi, Artificial neural network (ANN) approach for modeling and formulation of phenol adsorption onto activated carbon, *J. Eng. Thermophys.* 22 (4) (2013) 322–336.  
<https://doi.org/10.1134/S181023281304005X>
- 24- H.A.M. Ali, E.F.M. El-Zaidia, R.A. Mohamed, Experimental investigation and modeling of electrical properties for phenol red thin film deposited on silicon using back propagation artificial neural network, *Chinese Journal of Physics* 67(2020) 602-614  
<https://doi.org/10.1016/j.cjph.2020.07.018>
- 25- R.A. Mohamed, Prediction of AC conductivity for organic semiconductors based on artificial neural network ANN model, *Mater. Res. Express* 6 (2019) 085107  
<https://doi.org/10.1088/2053-1591/ab250a/meta>
- 26- A.S. Oladipo, O.A. Ajayi, A.A. Oladipo, S.L. Azarmi, Y. Nurudeen, A.Y. Atta, S.S. Ogunyemi, Magnetic recyclable eggshell-based mesoporous catalyst for biodiesel production from crude neem oil: Process optimization by central composite design and artificial neural network, *Comptes Rendus Chimie*, 21 (2018) 684  
<https://doi.org/10.1016/j.crci.2018.03.011/>
- 27- J. Ge, B. Sahiner, L. M. Hadjiiski, H. P. Chan, J. Wei, M. A. Helvie, C. Zhou, Computer aided detection of clusters of microcalcifications on full field digital mammograms, *Medical Physics* 33(8)((2006) 2975-2988  
<https://doi.org/10.1118/1.2211710>
- 28- C. Y. Chang, P. C. Chung, Two-layer competitive based Hopfield neural network for medical image edge detection, *Optical Engineering*, 39(3) (2000) 695-703.  
<https://doi.org/10.1117/1.602416>
- 29- S. Kobashi, N. Kamiura, Y. Hata, F. Miyawaki, Volume-quantization-based neural network approach to 3D MR angiography image segmentation, *Image and Vision Computing*, 19(4) (2001) 185-193.  
[https://doi.org/10.1016/S0262-8856\(00\)00067-6](https://doi.org/10.1016/S0262-8856(00)00067-6)
- 30- G. Stalidis, N. Maglaveras, S. N. Efstratiadis, A. S. Dimitriadis, C. Pa Model-based processing scheme for quantitative 4-D cardiac MRI analysis, *ppas, IEEE Trans. Information Technology In Biomedicine*, 6(1) (2002)59-72.  
<https://doi.org/10.1109/4233.992164>

- 31- M.S. Amir Faiz, C.A. Che Azurahamanima, S.A. Raba'aha, M.Z. Ruzniza, Low cost and green approach in the reduction of graphene oxide (GO) using palm oil leaves extract for potential in industrial applications, *Results in Physics* 16 (2020) 102  
<https://doi.org/10.1016/j.rinp.2020.102954>
- 32- S. El-Gamal and A. M. Ismail, Electrical and optical properties of novel brilliant cresyl blue dye-doped poly(methyl methacrylate) as selective cut-off laser filters, *Polymer International*, 69 (2020) 1308.  
<https://doi.org/10.1002/pi.6082>
- 33- A.M. Ismail, N.B. Gad Elmoulaa, R.M. El Shazly, A. Ashry, Impact of BaTiO<sub>3</sub> on the structural, optical, and nuclear radiation shielding parameters of poly(methyl methacrylate) nanocomposites as transparent shielding material, *Radiation Physics and Chemistry* 212 (2023) 111100.  
<https://doi.org/10.1016/j.radphyschem.2023.111100>
- 34- S Sain, D Ray, A Mukhopadhyay, S Sengupta, T Kar, CJ Ennis, PKSM Rahman, Synthesis and characterization of PMMA-cellulose nanocomposites by in situ polymerization technique, *J Appl Polym Sci* 126(S1):E127 (2012).  
<https://doi.org/10.1002/app.36723>
- 35- VV Soman, DS Kelkar, FTIR Studies of Doped PMMA - PVC Blend System, *Macromol. Symp.* 277(1) (2009)152.  
<https://doi.org/10.1002/masy.200950319>
- 36- VN Rai, C Mukherjee, B Jain, UV-Vis and FTIR spectroscopy of gamma irradiated polymethyl methacrylate, *Indian J. Pure App. Phys.*, 55 (2017) 775.  
<http://op.niscpr.res.in/index.php/IJPAP/article/viewFile/15541/1383>
- 37- P Maji, RB Choudhary, M Majhi, Structural, electrical and optical properties of silane-modified ZnO reinforced PMMA matrix and its catalytic activities, *J. Non-Crystal Solids*, 456 (2017) 40.  
<https://doi.org/10.1016/j.jnoncrysol.2016.10.039>
- 38- A.M. Ismail, M.I. Mohammed, I.S. Yahia, A facile method to prepare g-carbon nitride/poly(vinyl alcohol) nanocomposite films with remarkable optoelectrical properties: Laser attenuation approach, *Optics and Laser Technology*, 134 (2021) 106600.  
<https://doi.org/10.1016/j.optlastec.2020.106600>
- 39- G. Sahoo, N. Sarkar, D. Sahu, S.K. Swain, Nano gold decorated reduced graphene oxide wrapped polymethylmethacrylate for supercapacitor applications, *RSC Adv.* 7 (4) (2017) 2137–2150.  
<https://doi.org/10.1039/C6RA26930C>
- 40- U. Abaci, H.Y. Guney, M. Yilmazoglu, Plasticizer effect on dielectric properties of poly(methyl methacrylate)/titanium dioxide composites, *Polym. Compos.* 29 (2021) S565–S574.  
<https://doi.org/10.1177/096739112111014757>

**R. A. Mohamed et al.**

- 41- J.C.M. Costa, C.S. Ferreira, Y.F. Silva, M.R. Cunha, J.C.M. de Neto, V.M. Giacon, L. A. Pocrifka, Electrochemical nanoarchitectonics and analysis of PMMA/NiO based on electrochemical impedance spectroscopy, *Mater. Sci. Eng. B* 283 (2022) 115833.  
<https://doi.org/10.1016/j.mseb.2022.115833>
- 42- M. Huo, M. Ma, Y. Teng, Y. Xiao, Y. Guo, Suppressed physical aging in PMMA-titanium oxide nanocomposites by controlling alignment of nanoparticles, *J. Appl. Polym. Sci.* (2023) e54030.  
<https://doi.org/10.1002/app.54030>
- 43- D.A. Nasrallah, E.G. El-Metwally, A.M. Ismail, Structural, thermal, and dielectric properties of porous PVDF/Li<sub>4</sub>Ti<sub>5</sub>O<sub>12</sub> nanocomposite membranes for high-power lithium-polymer batteries, *Polymers for Advanced Technologies*, 32 (2021) 1214-1229.  
<https://doi.org/10.1002/pat.5171>
- 44- A. Abou Elfadl, A. M. Ismail, M. I. Mohammed, Dielectric study and AC conduction mechanism of gamma irradiated nano-composite of polyvinyl alcohol matrix with Cd<sub>0.9</sub>Mn<sub>0.1</sub>S, *J. of Materials Science: Materials in Electronics* 31 (2020) 8297.  
<https://doi.org/10.1007/s10854-020-03365-z>
- 45- M.H. Hamsan, A.A. Azli, S.B. Aziz, N.A. Shamsuri, M.F.Z. Kadir, N.S. Nazri, L.K. Keng, H.F.M. Zaid, M.F. Shukur, Characterization of methylcellulose based composite polymer electrolytes reinforced with Reduced-Graphene oxide, *Materials Science & Engineering B* 303 (2024) 117313.  
<https://doi.org/10.1016/j.mseb.2024.117313>
- 46- Zhou DF, Yuan H, Xiong YL, Luo GQ, Shen Q, Constructing highly directional multilayer cell structure(HDMCS) towards broadband electromagnetic absorbing performance for CNTs/PMMA nanocomposites foam, *Compos Sci Technol*, 203 (2021)108614.  
<https://doi.org/10.1016/j.compscitech.2020.108614>
- 47- M. I. Mohammed, H. Y. Zahran, S. Zyoud, I. S. Yahia, A.M. Ismail, Simple processed polyvinyl alcohol/multi-wall carbon nanotube polymeric nanocomposites for high-performance optoelectronics, *Journal of Materials Science: Materials in Electronics* 35 (2024) 515.  
<https://doi.org/10.1007/s10854-024-12144-z>
- 48- S. Choudhary, R. J. Sengwa, Investigation on Structural and Dielectric Properties of Silica Nanoparticles Incorporated Poly(Ethylene Oxide)/Poly(Vinyl Pyrrolidone) Blend Matrix Based Nanocomposites, *J. Inorg. Organometal. Polym. Mater.* 29 (2019) 592-607.  
<https://doi.org/10.1007/s10904-018-1034-1>
- 49- A. M. Gaur, D. S. Rana, *J. Mater. Sci.*, Effect of CoCl<sub>2</sub>-BaCl<sub>2</sub> fillers on morphology, dielectric constant and conductivity of PVDF composite for pressure sensing application, *Mater. Electron.* 27 (2016) 2293-2299.  
<https://doi.org/10.1007/s10854-015-4024-x>

- 50- R. J. Sengwa and S. Choudhary, Dielectric and electrical properties of PEO–Al<sub>2</sub>O<sub>3</sub> nanocomposites, *J. Alloys Compd.* 701 (2017) 652-659.  
<https://doi.org/10.1016/j.jallcom.2017.01.155>
- 51- F. Mao, Z. Shi, J. Wang, C. Zhang, C. Yang, M. Huang, Improved dielectric permittivity and retained low loss in layer-structured films via controlling interfaces, *Adv. Compos. Hybrid Mater.* 1 (2018) 548-557.  
<https://doi.org/10.1007/s42114-018-0041-6>
- 52- N. S. Alghunaim and H. M. Alhusaiki-Alghamdi, Role of ZnO nanoparticles on the structural, optical and dielectric properties of PVP/PC blend, *Physica B* 560 (2019) 185-190.  
<https://doi.org/10.1016/j.physb.2019.02.021>
- 53- R. S. Hafez, N. A. Hakeem, A. A. Ward, A. M. Ismail and F. H. Abd El kader, Dielectric and Thermal Properties of PEO/PVDF Blend Doped with Different Concentrations of Li<sub>4</sub>Ti<sub>5</sub>O<sub>12</sub> Nanoparticles, *J. Inorg. Organomet. Polym.* (2020).  
<https://doi.org/10.1007/s10904-020-01637-z>
- 54- Y. Zhai, K. Xiao, J. Yu, J. Yang, B. Ding, Thermostable and nonflammable silica–polyetherimide–polyurethane nanofibrous separators for high power lithium ion batteries, *Mater. Chem. A* 3 (2015) 10551-10558.  
<https://pubs.rsc.org/en/content/articlelanding/2015/ta/c5ta00856e/unauth>
- 55- S. El-Gamal, A. M. Ismail, R. El-Mallawany, Dielectric and nano-scale free volume properties of polyaniline/polyvinyl alcohol nanocomposites, *J. Mater. Sci.: Mater. Electron.* 26 (2015) 7544-7553.  
<https://doi.org/10.1007/s10854-015-3391-7>
- 56- S.R. Elliott, A.c. conduction in amorphous chalcogenide and pnictide semiconductors, *Adv. Phys.* 36 (1987) 135-217.  
<https://doi.org/10.1080/00018738700101971>
- 57- S. R. Elliott, Temperature dependence of a.c. conductivity of chalcogenide glasses, *Philos. Mag. B* 37 (1978) 553-560.  
<https://doi.org/10.1080/01418637808226448>
- 58- N. F. Mott, E. A. Davis, R. A. Street, States in the gap and recombination in amorphous semiconductors, *Philos. Mag.* 32 (1975) 961-996.  
<https://doi.org/10.1080/14786437508221667>
- 59- L. G. Austin, N. F. Mott, Polarons in crystalline and non-crystalline materials, *Adv. Phys.* 18 (1969) 41-102.  
<https://doi.org/10.1080/00018736900101267>
- 60- T. Mahapatra, S. Halder, S. Bhuyan, R. N. P. Choudhar, Dielectric and electrical characterization of lead-free complex electronic ceramic: (Bi<sub>1/2</sub>Li<sub>1/2</sub>)(Zn<sub>1/2</sub>W<sub>1/2</sub>)O<sub>3</sub>, *J. Mater. Sci.: Mater. Elect.* 29 (2018) 18742-18750.  
<https://doi.org/10.1007/s10854-018-9998-8>
- 61- S. Choudhary, Dielectric dispersion and relaxations in (PVA-PEO)-ZnO polymer nanocomposites, *Physica B* 522 (2017) 48-56.

**R. A. Mohamed et al.**

<https://doi.org/10.1016/j.physb.2017.07.066>

62- G. E. Pike, ac Conductivity of Scandium Oxide and a New Hopping Model for Conductivity, Phys. Rev. B 6 (1972) 1572-1580.

<https://doi.org/10.1103/PhysRevB.6.1572>

63- S. Ishaqa, F. Kanwala, S. Atiq, M. Moussa, U. Azhar, I. Guld, D. Losic, Dielectric and impedance spectroscopic studies of three phase graphene/titania/poly(vinyl alcohol) nanocomposite films, Results in Physics 11 (2018) 540-548.

<https://doi.org/10.1016/j.rinp.2018.09.049>

Egypt J. Solids, Vol. (47) (2025)